ADVANCES IN ATMOSPHERIC SCIENCES, VOL. 38, JULY 2021, 1209–1222

• **Original Paper** •

RO_x Budgets and O_3 Formation during Summertime at Xianghe Suburban Site in the North China Plain

Min XUE*[1], Jianzhong MA[1], Guiqian TANG[2], Shengrui TONG[3], Bo HU[2], Xinran ZHANG[3], Xinru LI[4], and Yuesi WANG*[2]

[1]*State Key Laboratory of Severe Weather & China Meteorological Administration Key Laboratory of Atmospheric Chemistry*, *Chinese Academy of Meteorological Sciences*, *Beijing* 100081, *China*

[2]*State Key Laboratory of Atmospheric Boundary Layer Physics and Atmospheric Chemistry*, *Institute of Atmospheric Physics*, *Chinese Academy of Sciences*, *Beijing* 100029, *China*

[3]*State Key Laboratory for Structural Chemistry of Unstable and Stable Species*, *Beijing National Laboratory for Molecular Sciences*, *Chinese Academy of Sciences Research/Education Center for Excellence in Molecular Sciences*, *Institute of Chemistry*, *Chinese Academy of Sciences*, *Beijing* 100190, *China*

[4]*Department of Chemistry*, *Capital Normal University*, *Beijing* 100081, *China*

(Received 27 September 2020; revised 14 December 2020; accepted 26 February 2021)

ABSTRACT

Photochemical smog characterized by high concentrations of ozone (O_3) is a serious air pollution issue in the North China Plain (NCP) region, especially in summer and autumn. For this study, measurements of O_3, nitrogen oxides (NO_x), volatile organic compounds (VOCs), carbon monoxide (CO), nitrous acid (HONO), and a number of key physical parameters were taken at a suburban site, Xianghe, in the NCP region during the summer of 2018 in order to better understand the photochemical processes leading to O_3 formation and find an optimal way to control O_3 pollution. Here, the radical chemistry and O_3 photochemical budget based on measurement data from 1–23 July using a chemical box model is investigated. The daytime (0600–1800 LST) average production rate of the primary radicals referred to as RO_x (OH + HO_2 + RO_2) is 3.9 ppbv h^{-1}. HONO photolysis is the largest primary RO_x source (41%). Reaction of NO_2 + OH is the largest contributor to radical termination (41%), followed by reactions of RO_2 + NO_2 (26%). The average diurnal maximum O_3 production and loss rates are 32.9 ppbv h^{-1} and 4.3 ppbv h^{-1}, respectively. Sensitivity tests without the HONO constraint lead to decreases in daytime average primary RO_x production by 55% and O_3 photochemical production by 42%, highlighting the importance of accurate HONO measurements when quantifying the RO_x budget and O_3 photochemical production. Considering heterogeneous reactions of trace gases and radicals on aerosols, aerosol uptake of HO_2 contributes 11% to RO_x sink, and the daytime average O_3 photochemical production decreases by 14%. The O_3-NO_x-VOCs sensitivity shows that the O_3 production at Xianghe during the investigation period is mainly controlled by VOCs.

Key words: photochemical smog, RO_x budgets, O_3 production rate, O_3 chemical regime

Citation: Xue, M., J. Z. Ma, G. Q. Tang, S. R. Tong, B. Hu, X. R. Zhang, X. R. Li, and Y. S. Wang, 2021: RO_x budgets and O_3 formation during summertime at Xianghe Suburban Site in the North China Plain. *Adv. Atmos. Sci.*, **38**(7), 1209–1222, https://doi.org/10.1007/s00376-021-0327-4.

Article Highlights:

- HONO photolysis is the dominant primary RO_x source, accounting for 41% of the daytime average.
- Sensitivity tests without the HONO constraint highlight the importance of measuring HONO in solving the RO_x budget and analyzing O_3 photochemical production.
- The O_3-NO_x-VOCs sensitivity shows that O_3 production is mainly controlled by VOCs at Xianghe during the investigation period.

1. Introduction

Photochemical smog has become a serious air pollution issue in urban and industrial centers in recent decades

* Corresponding authors: Min XUE, Yuesi WANG
Email: xuem@cma.gov.cn, wys@mail.iap.ac.cn

(Molina and Molina, 2004; Zhang et al., 2008; Monks et al., 2009; Wang et al., 2017). O_3 is one of the major contributors to photochemical smog and is produced via photochemical reactions involving nitrogen oxides (NO_x = NO + NO_2), carbon monoxide (CO) and volatile organic compounds (VOCs). High concentrations of tropospheric O_3 affect human health, ecosystems, and climate (Molina et al., 2010; Monks et al., 2015). However, O_3 pollution is difficult to control, mainly because the photochemical production of O_3 has a nonlinear dependence on its precursors, NO_x and VOCs. The sensitivity of O_3 production to its precursors varies greatly from one region to another mainly due to diverse source types and emission rates of NO_x and VOCs. Therefore, understanding the photochemical processes leading to O_3 formation is critical for efficient ozone pollution control.

The hydroxyl radical (OH), hydroperoxy radical (HO_2), and organic peroxy radical (RO_2), collectively referred to as RO_x, control the removal of primary pollutants and formation of secondary pollutants such as O_3 and secondary aerosols (Hofzumahaus et al., 2009; Stone et al., 2012). OH is primarily produced by photolysis of O_3, nitrous acid (HONO), and hydrogen peroxide (H_2O_2), as well as alkene ozonolysis reactions (Levy, 1971; Ehhalt, 1999; Ma et al., 2012). As the most reactive oxidant, OH initiates the oxidation reactions of most primary pollutants in the atmosphere. OH reacts with CO and VOCs to produce HO_2 and RO_2 radicals, respectively. RO_2 is converted to HO_2 by reacting with NO. HO_2 further reacts with NO to recycle OH. The recycling reactions between OH, HO_2, and RO_2 in the presence of VOCs and NO_x lead to the catalytic cycle between NO and NO_2 and eventually result in net production of O_3 (Kuhn et al., 2010). RO_x radicals are ultimately removed by reacting with NO_x under high NO_x levels to produce nitric acid (HNO_3) and organic nitrates (RO_2, NO_2, and $RONO_2$), or by self-reactions under low NO_x levels to produce peroxides (H_2O_2 and ROOH). RO_x chemistry has been a focus in understanding O_3 photochemical processes. A number of studies have investigated RO_x budgets for areas all over the world with varying characteristics, such as polluted urban and suburban areas (Ren et al., 2003; Emmerson et al., 2005a; Sheehy et al., 2010; Volkamer et al., 2010; Ma et al., 2012; Xue et al., 2016), rural areas (Hofzumahaus et al., 2009; Lu et al., 2012; Tan et al., 2017), and remote areas (Kubistin et al., 2010; Lelieveld, 2010; Mao et al., 2010).

The North China Plain (NCP) is one of the most industrialized and urbanized regions in eastern China. Photochemical smog characterized by high concentrations of O_3 has been regarded as the most prevalent air pollution issue in the NCP on the regional scale (Ma et al., 2012; Wang et al., 2017). With increased emissions mitigation since the 2000s, primary pollutant levels have declined, but O_3 concentrations have experienced an increasing trend in both urban, background and mountainous areas (Tang et al., 2009; Zhang et al., 2014; Ma et al., 2016; Sun et al., 2016; Lu et al., 2018; Li et al., 2019). The formation mechanism of O_3 pollution in the NCP has been investigated by numerous studies in last two decades. Most studies have focused on the impact of urban plumes on O_3 pollution at the regional scale (Wang et al., 2006; Lin et al., 2008; Ma et al., 2013; Xue et al., 2013), local production and regional transport contributions (Streets et al., 2007; Wang et al., 2009; Wu et al., 2017), precursor-O_3 relationships (Shao et al., 2009; Lu et al., 2010; Tang et al., 2012), and O_3 source attributions (Qu et al., 2014; Li et al., 2017; Lu et al., 2019). Some studies have investigated radical sources and atmospheric oxidizing capacity to understand ozone photochemical processes using an observation-based modeling approach (Liu et al., 2012; Ma et al., 2012; Tan et al., 2019). Liu et al. (2012) analyzed RO_x budgets and O_3 photochemistry for summertime in Beijing and found that photolysis of oxygenated VOC (OVOC) and HONO was the dominant primary RO_x source, which resulted in high production of O_3. Ma et al. (2012) investigated the HO_x and O_3 photochemical process and concluded that the lower atmosphere over the NCP was highly polluted and served as an oxidation pool, under which primary pollutants were quickly oxidized. Tan et al. (2019) reported that HONO and HCHO photolysis contributed about 50% of the total primary RO_x source in Beijing and high atmospheric oxidation capacity led to O_3 pollution in Chinese megacities. Most studies concentrated on Beijing urban areas, and only a few focused on its surrounding suburban areas (Lu et al., 2013; Tan et al., 2017). In addition to Beijing, O_3 pollution is serious at its surrounding area, such as Xianghe site, with the highest frequency of exceeding national air quality thresholds (Tang et al., 2012). However, the radical chemistry and photochemical processes leading to O_3 formation for the Xianghe site have not yet been documented, and therefore must be investigated in order to illustrate the underlying chemical mechanism of O_3 pollution on a regional scale.

For this study, measurements of O_3 and its precursors were taken at the Xianghe suburban site in the NCP region during the summer of 2018 and used to constrain a chemical box model in order to investigate the radical budget and O_3 photochemistry of the region. A description of the observation site and measurements and an introduction of the chemical box model are given in section 2. Then, an analysis of the observation data taken over the period of 1–23 July is given, and the modeling analysis results, including the RO_x radical budgets and O_3 production/loss rates, as well as their sensitivities to NO_x, VOCs, HONO, and heterogeneous reactions on aerosols are presented in section 3. Finally, conclusions are provided in section 4.

2. Methods

2.1. *Sampling site and measurements*

The field campaign was conducted at the Xianghe Atmospheric Observatory (39.798°N, 116.958°E; 35 m above sea level) during the summer of 2018. Xianghe is a typical suburban site, about 50 km, 75 km, and 35 km away from Beijing, Tianjin, and Langfang in Hebei province, respectively. The site is surrounded by agricultural land and residen-

tial areas. The downtown center (population of about 30 000) is about 4 km east of the site.

Trace gases (including O_3, NO_x, and CO) were measured by commercial instruments from Thermo Fisher Scientific, USA. The instruments were located on the roof of a single-story building. O_3, NO_x, and CO were continuously measured using the O_3 analyzer (Model 49i), the NO-NO_2-NO_x chemiluminescence analyzer (Model 42i), and the CO analyzer (Model 48i), respectively. The precision and accuracy, operation and maintenance, and calibration methods for these instruments have previously been described in detail (Ji et al., 2014). Ambient VOC samples were analyzed continuously using a gas chromatography (GC) instrument (7820A, Agilent Technologies, Santa Clara, CA, USA) equipped with a mass spectrometer (MS) and a flame ionization detector (FID) (5977E, Agilent Technology, Santa Clara, CA, USA) with a time resolution of 1 h. Detailed description of the GC-MS/FID analysis method can be found in Wang et al. (2014). Dual columns and detectors were applied for the simultaneous analysis of C2–C12 hydrocarbons. The VOCs measurements include C2–C12 alkanes, C2–C6 alkenes, and C6–C10 aromatics. HONO was measured using a custom-made HONO analyzer, which was described in detail by Hou et al. (2016). Briefly, the principle of a HONO analyzer is similar to a long path absorption photometer (LOPAP) (Kleffmann et al., 2002). Information about detection limit and data accuracy are presented in Table S1 in the electronic supplementary material (ESM). Further details about the instruments including their operation and calibration procedures are available in the supplemental material.

The photolysis frequencies (JO^1D, JNO_2, JHONO, JH_2O_2, JHCHO, and JNO_3) were measured using a PFS-100 spectroradiometer (Focused Photonics Inc., Hangzhou, China), which was described in detail by Zhao et al. (2021). The mixing layer height was observed by ceilometer (CL31, Vaisala, Finland), described in detail by Tang et al. (2016). Other meteorological parameters, such as the ambient temperature, pressure, and relative humidity were simultaneously measured at the Xianghe Atmospheric Observatory. Measurement results from 1–23 July, the period during the experiment when the photochemical pollution was the most severe, are presented in this paper. The time series of meteorological parameters are shown in Fig. S1 in the ESM.

2.2. *Chemical box model*

A box model was used to explore the radical budget and O_3 photochemical formation and loss. The model is built on the NCAR Master Mechanism (Madronich and Calvert, 1990; Ma et al., 2002, 2012), which is an explicit gas phase chemical mechanism and calculates the local photochemical equilibrium with a time scale of several minutes. In addition, heterogeneous reactions of trace gases and radicals on aerosol surfaces were also incorporated in the model (see section 2.2 of Ma et al., 2012). Meanwhile, dry deposition and entrainment losses were also included in the model to account for the physical loss processes. The model was constrained by the concentrations of measured trace gases, including inorganic species (H_2O, NO, NO_2, O_3, HONO, and CO) and VOCs. The observed individual VOC species (Table S2 in the ESM) were applied to the model simulations in the same way as used by Ma et al. (2012). Measurements of photolysis frequencies, mixing layer height, and meteorological parameters were also used to constrain the model simulations.

The measured data were averaged or interpolated with a time resolution of 1 hour for the model constraints. Simulations were performed for the time period from 1–23 July starting at 0000 LST (LST = UTC + 8), with a five-day pre-run in advance to let the unconstrained compounds to reach steady state, and then the results after that were used for analyses. The model calculates radical concentrations and chemical reaction rates, which can be used to further quantify radical budget and O_3 photochemical production. The uncertainty of model calculation consists of uncertainty of the measurements used to constrain the model and uncertainty of the kinetic reaction rate. OVOCs concentrations were simulated by the model. The mean observed concentration of HCHO was 1.2 ± 0.9 ppbv for the period from Nov 2017 to Jan 2018 at Xianghe (Tang et al., 2019) and 4.4 ± 1.6 ppbv in July 2018 (X. R. LI, personal communication). The mean simulated HCHO concentrations in our study was 3.7 ± 1.3 ppbv, comparable to the other observed results at the same site.

3. Results and discussion

3.1. *Observed O_3 and precursor analysis*

Figure 1 presents the mean diurnal variations of measured NO_x, CO, HONO, AVOC (anthropogenic VOC), isoprene, O_3, and O_x (O_3+NO_2). The primary anthropogenic pollutants including NO_x, CO, and AVOC have similar diurnal variations and all reach a maximum in the early morning and a minimum in the afternoon. The maximum in the morning is related to gasoline and diesel vehicle exhaust (Tang et al., 2019) during rush hour coinciding with a shallow planetary boundary layer (PBL). In the afternoon, the pollutants decrease to minimum due to strong dilution with the development of the PBL. During the nighttime, the pollutants tend to accumulate when the PBL decreases. HONO has a similar variation pattern as NO_2. Heterogeneous reactions of NO_2 are expected to be the most important source of HONO (Liu et al., 2021) and a good correlation between HONO and NO_2 during different field studies has been reported by Elshorbany et al. (2012). In this study, the averaged daytime HONO concentration is about 0.9 ppbv, comparable to those observed in Beijing (Lu et al., 2010) and Hong Kong (Xue et al., 2016), and higher than observations reported in New York (Ren et al., 2003) and Birmingham (Emmerson et al., 2005b). Isoprene emissions include both biogenic and anthropogenic sources. Biogenic emissions have a good correlation with temperature. Different to the diurnal variation of AVOC, the diurnal maximum of isoprene occurrs in the

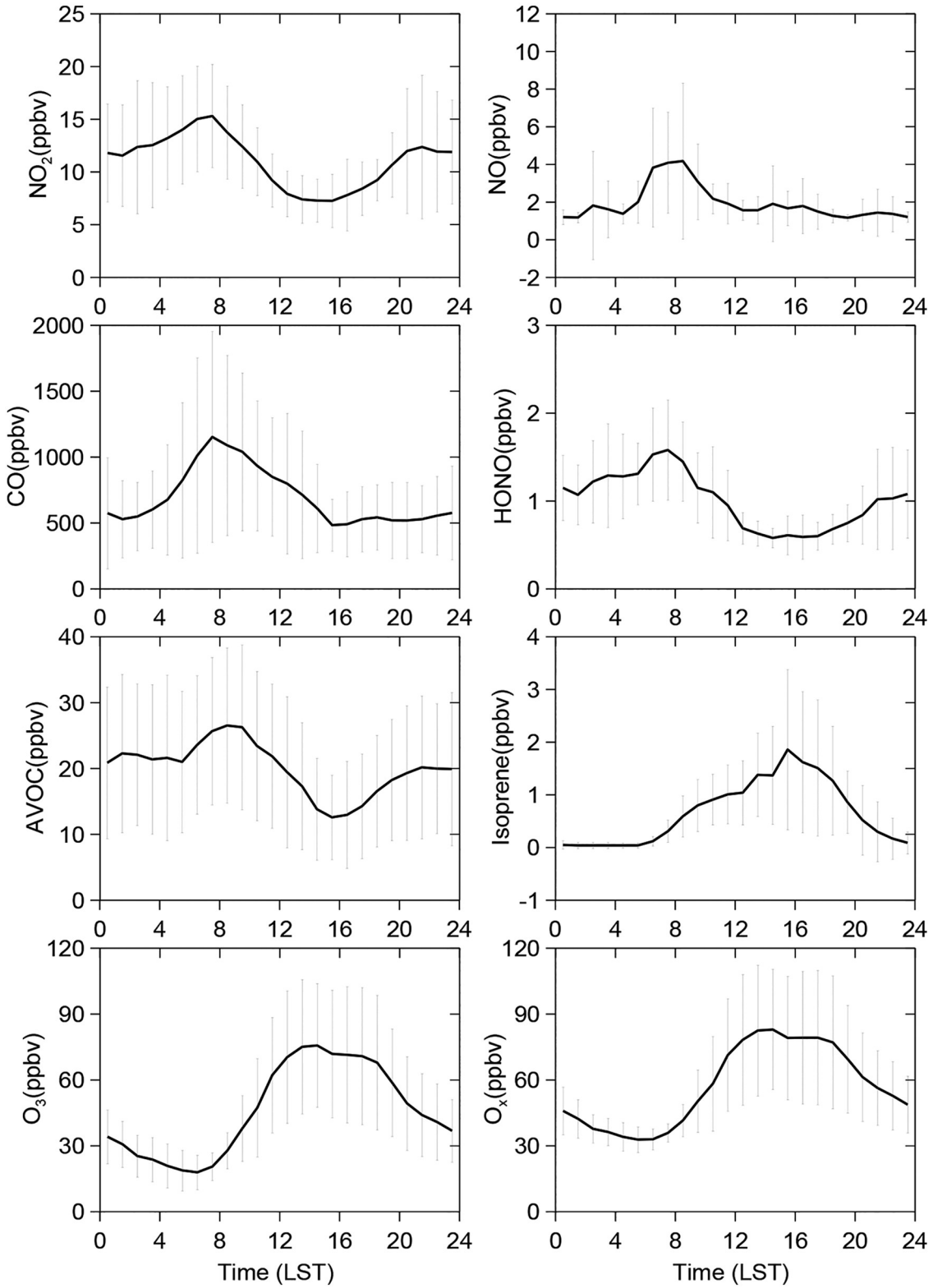

Fig. 1. Averaged diurnal variations of measured NO_x, CO, HONO, AVOC, isoprene, O_3, and O_x at the Xianghe site. The vertical bars show the hourly standard deviation.

afternoon (1500 LST), indicating that isoprene is mostly from biogenic rather than anthropogenic emissions at the Xianghe site.

O_3 has a variation pattern that is typical for photochemical pollution with a maximum around 76 ppbv in the afternoon. The hourly maximum O_3 is 136 ppbv, much higher than the Chinese National Air Quality Standard Grade II, indicating serious O_3 pollution at the Xianghe site. During

the daytime, with incoming solar radiation, the rapid chemical cycle between NO, NO_2, and O_3 converts some O_3 to NO_2. Therefore, total oxidant O_x, the sum of O_3 and NO_2, is used to indicate O_3 pollution, especially in the urban and suburban areas where NO concentrations are high (Liu et al., 1987; Lu et al., 2010). The mean O_x diurnal profile shows a maximum value of 83 ppbv. Mean concentrations plus/minus standard deviations of O_3, O_x, NO, NO_x, CO, HONO, isoprene, and AVOC were 46.1 ± 28.8 ppbv, 57.2 ± 26.5 ppbv, 1.9 ± 1.8 ppbv, 13.0 ± 6.0 ppbv, 694.6 ± 478.1 ppbv, 1.0 ± 0.5 ppbv, 0.7 ± 0.9 ppbv, and 20.0 ± 11.0 ppbv, respectively.

From field campaign data, 56 VOC species including alkanes, alkenes, aromatics, and isoprene are quantitatively identified. The reactivity of individual VOC species is calculated using observed VOC concentration multiplied by its corresponding reaction rate constant with OH at 298 K (Atkinson and Arey, 2003). Figure 2 shows the percentage contributions of alkanes, alkenes, aromatics, and isoprene to measured total VOC concentration and calculated total VOC reactivity. The average mixing ratio and reactivity of total VOC at Xianghe are 20.7 ppbv and 4.3 s^{-1}, respectively, comparable to the values observed at Yufa suburban site (39.514°N, 116.305°E) in Beijing in summer 2006 (Shao et al., 2009; Lu et al., 2010), and much lower than results (41.8 ppbv and 15.8 s^{-1}) measured at the Shangdianzi (SDZ) regional background station (40.650°N, 117.117°E) for summertime of 2007 (Xu et al., 2011). The difference between Xianghe and SDZ could be caused by different sampling times (samples on each Tuesday at 0800–0830 LST and 1400–1430 LST were measured at SDZ, see section 2.2 of Xu et al., 2011). As shown in Fig. 2a, alkanes contribute 62.2% to the total VOC mixing ratio. The contributions of alkenes and aromatics are the same with the value of 17.3%, and isoprene only contributes 3.2%. According to Lu et al. (2010), the contributions of alkanes, alkenes, aromatics and isoprene to the total VOC mixing ratio at the Yufa site were 53%, 24%, 21%, and 2%, respectively, with higher contributions of alkenes and aromatics than results at Xianghe. With respect to the reactivity, however, isoprene accounts for 38.6% of the measured VOC reactivity, higher than that of alkenes, aromatics, and alkanes. The contributions of alkenes and aromatics groups are comparable, with a slightly different portion of 21.1% and 24.7%, respectively, and alkanes only account for 15.6%. The above results indicate the high reactivity of isoprene at this suburban site.

3.2. *Modeled OH reactivity*

The total OH reactivity (K_{OH}), equivalent to the inverse of the OH lifetime, is defined as the pseudo-first-order rate coefficient of OH radical in ambient atmosphere. The K_{OH} is calculated by the following equation (Lou et al., 2010; Mao et al., 2010):

$$K_{OH} = \sum_i K_{OH+X_i}[X_i] \ , \qquad (1)$$

where $[X_i]$ is the ambient concentration of individual reactive species (NO_x, CO, VOCs, and OVOC, etc.), K_{OH+X_i} is the rate coefficient of the reaction between X_i and OH radical, and $K_{OH+X_i}[X_i]$ represents the reactivity of X_i. Figure 3a shows the average diurnal variation of K_{OH} calculated with the box model, including the reactivity of measured CO, NO_x, alkanes, alkenes, aromatics, isoprene, and model simulated other secondary species (HCHO, acetaldehyde, acetone, etc.). The K_{OH} ranges between 12 s^{-1} and 18 s^{-1}, with the maximum value occurring around 0800 LST (the morning rush hour), which is similar to the diurnal variation pattern shown in previous studies (Lou et al., 2010; Fuchs et al., 2017). The diurnal profile of OH reactivity is relatively

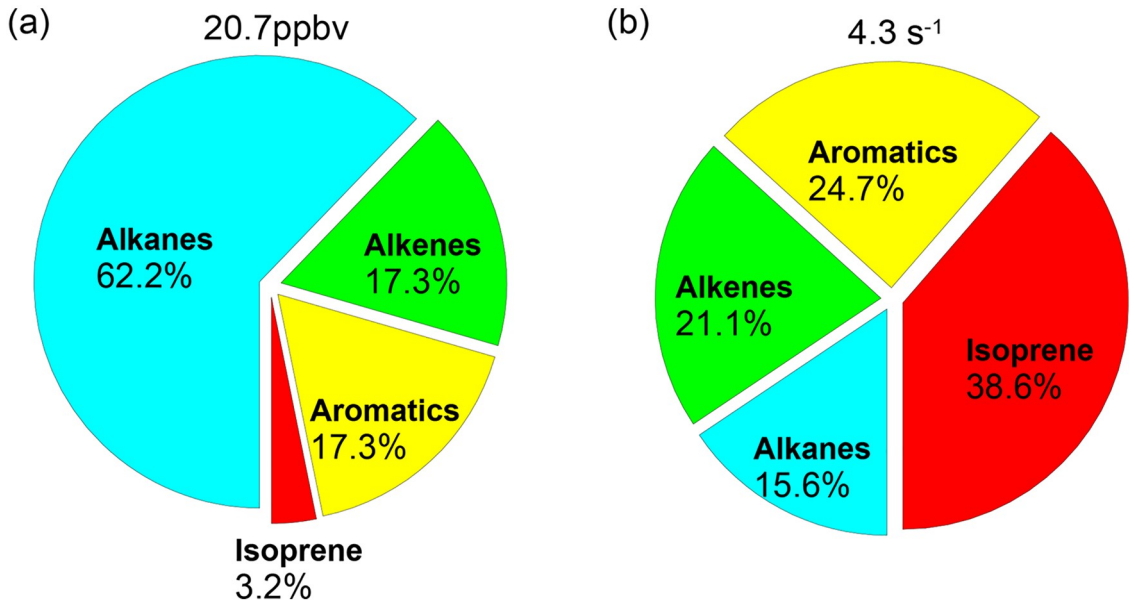

Fig. 2. Percentage contributions of alkane, alkene, aromatic, and isoprene to measured VOC concentration (a) and reactivity (b) at the Xianghe site.

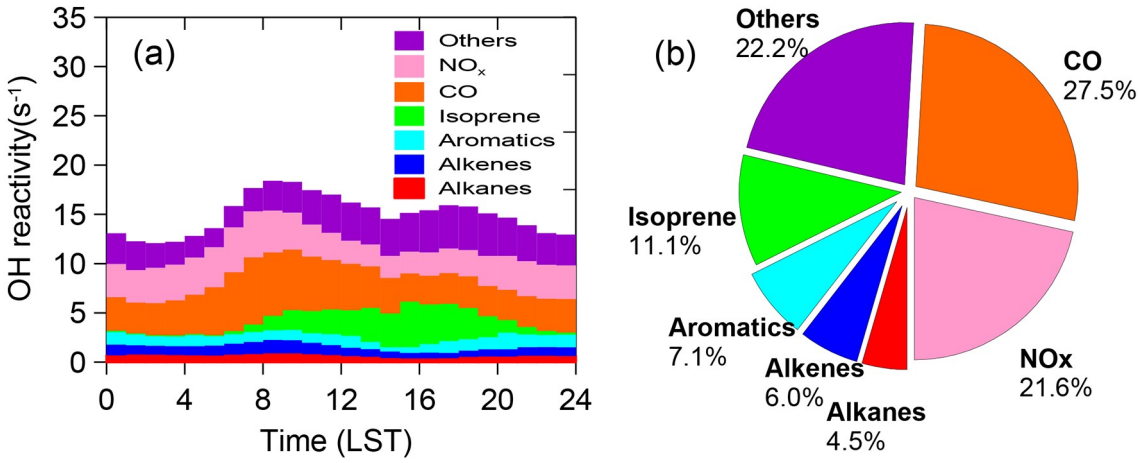

Fig. 3. Averaged diurnal variations of the contributions from all measured species and model generated species (denoted as Others) (a). Percent contributions of all measured species and model generated species to the total OH reactivity (b).

flat, with less decrease than reactive gas concentrations during daytime, because of the high contribution of isoprene in the afternoon.

Over the past two decades, direct measurements of K_{OH} have been performed in different regions, such as New York (Ren et al., 2003), Mexico (Shirley et al., 2006), Paris (Dolgorouky et al., 2012), Guangzhou (Lou et al., 2010; Yang et al., 2017), and Beijing (Lu et al., 2013; Williams et al., 2016). According to the observed results from Guangzhou (Lou et al., 2010; Yang et al., 2017), the K_{OH} values at a rural site, Backgarden (23.49°N, 113.03°E), in summer 2006 and a suburban site, Heshan (22.73°N, 112.93°E), in autumn 2014 were in the range of 20 to 50 s^{-1}. The K_{OH} was also measured at the Yufa site in summer 2006, with the average values falling in the range of 10–30 s^{-1} (Lu et al., 2013). At the rural Wangdu site (39.514°N, 116.305°E) in the NCP, the measured K_{OH} ranged between 10–20 s^{-1} in summer 2014 (Fuchs et al., 2017). The calculated OH reactivity at the Xianghe site is comparable to that measured at Wangdu in the NCP and lower than those observed in Guangzhou.

Figure 3b shows the percentage contributions of different species to the total OH reactivity. The sum of CO and NO_x accounts for 49.1% of total OH reactivity, with CO contributing 27.5% (4.1 s^{-1}) and NO_x contributing 21.6% (3.2 s^{-1}), respectively. The AVOCs, including alkanes, alkenes, and aromatics, contribute 17.6% to the total OH reactivity. The isoprene reactivity accounts for 11.1%. Model calculated other secondary species (HCHO, acetaldehyde, acetone, etc.) account for the remaining 22.2%. Our results show that the sum of VOCs and secondary species contributes to 50% of the total OH reactivity.

3.3. *Simulated RO_x radical concentrations*

Measurements of RO_x radicals in China are relatively rare. In this study, RO_x radical concentrations are calculated using the NCAR-MM chemical box model, constrained by the observed hourly gas concentrations and physical parameters. Figure 4 presents the mean diurnal variations of OH, HO_2, and RO_2 radicals at the Xianghe site. Radical concentrations show typical diurnal variations with a maximum occurring at noon. The maximum concentrations of OH, HO_2, and RO_2 in the averaged diurnal cycle at Xianghe are 10.6 × 10^6, 5.5 × 10^8, and 3.7 × 10^8 molecules cm^{-3}, respectively, comparable to those simulated at the Peking University campus (PKU) site in August 2007, with corresponding values of 9 × 10^6, 6.8 × 10^8, and 4.5 × 10^8 molecules cm^{-3} (Liu et al., 2012). According to the simulated hourly radical concentrations (Fig. S2 in the ESM), the daily maximums of OH, HO_2, and RO_2 at Xianghe have ranges of (4–17) × 10^6, (1–13) × 10^8, and (1–11) × 10^8 molecules cm^{-3}, respectively. Observed daily maximum concentrations of OH and HO_2 had ranges of (4–17) × 10^6 and (2–24) × 10^8 molecules cm^{-3} at the Yufa suburban site in August 2006 (Lu et al., 2013). Daily maximum OH, HO_2, and RO_2 concentrations were also observed with ranges of (5–15) × 10^6, (3–14) × 10^8 and (3–15) × 10^8 molecules cm^{-3}, respectively, at the Wangdu rural site in the NCP in summer 2014 (Tan et al., 2017). In contrast, higher daily maximum values of (15–26) × 10^6 molecules cm^{-3} for OH and (3–25) × 10^8 molecules cm^{-3} for HO_2 were observed at the Backgarden rural site in Guangzhou during July 2006 (Lu et al., 2012). The simulated RO_x concentrations in this study are comparable to observed values at Wangdu (Tan et al., 2017) and much lower than those at Backgarden (Lu et al., 2012).

Using the NCAR-MM chemical box model, HONO concentrations are calculated with the daytime average value being 0.08 ppbv, only about 10% of the measured result (0.9 ppbv). The large underestimation proportion of HONO in this study is consistent with previously reported results (Su et al., 2011; Tong et al., 2016; Liu et al., 2021), due to only considering homogeneous reactions of NO + OH and a lack of large sources such as heterogeneous reactions of NO_2 in the current chemical models. In order to estimate the impact of the missing HONO source on the radical chemistry at Xianghe, we calculate the RO_x concentrations

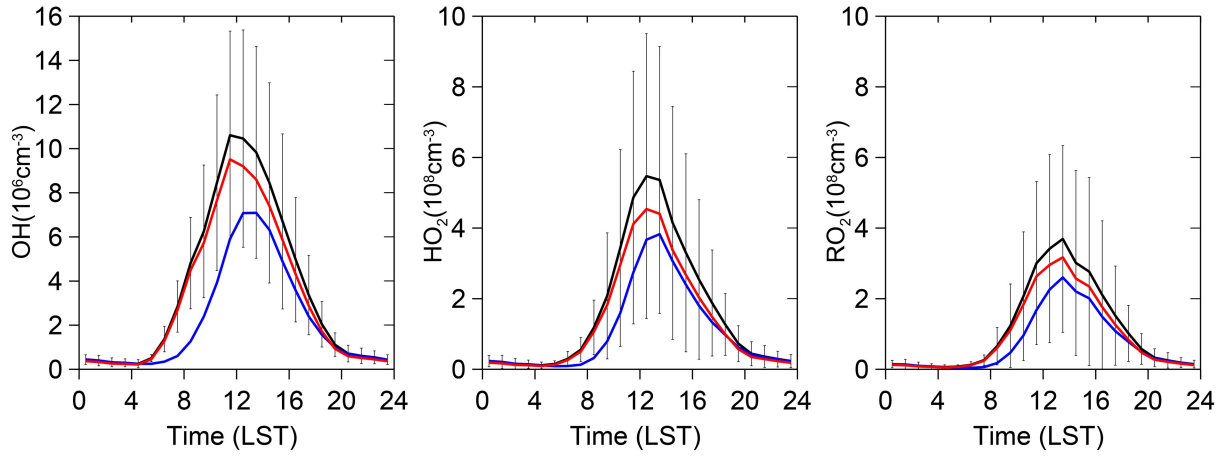

Fig. 4. Averaged diurnal variations of OH, HO_2, and RO_2 radical concentration modeled for the Xianghe site. Black lines represent the calculated concentrations with all measured gases as model constraint, and the vertical bars show the hourly standard deviation; Blue lines represent the sensitivity results without the HONO constraint; Red lines represent the sensitivity results considering heterogeneous reactions of gases and radicals on aerosols.

without the HONO constraint. The sensitivity simulation results show that the maximum concentrations of OH, HO_2, and RO_2 decrease to 7.2×10^6, 3.8×10^8, and 2.6×10^8 molecules cm^{-3}, respectively, as presented in Fig. 4. For daytime average (0600 to 1800 LST), the OH decreases by 41%. Decreasing OH leads to less active photochemistry and thus 38% and 37% decrease of HO_2 and RO_2 concentrations, respectively, in agreement with previous results (Su et al., 2011; Liu et al., 2012; Li et al., 2014; Tong et al., 2016). Therefore, the measured HONO data should be included to properly simulate the RO_x chemistry.

The aerosol size distributions, a key parameter for the calculation of heterogeneous reaction rates, are not measured at Xianghe. Regardless of the uptake coefficients and aerosol particle size distributions, the heterogeneous reaction rates are ultimately determined by the calculated pseudo first-order rate coefficients. So, we adopt the pseudo first-order rate coefficients from our previous study, which were calculated with the particle size distributions observed at the Xin'an rural site, about 60 km east of Xianghe (Ma et al., 2012). According to Ma et al. (2012), the calculated pseudo first-order rate coefficient of HO_2 was 0.025 s^{-1}, which could represent an upper limit since the observed $PM_{2.5}$ concentrations in that field campaign were more than twice those at Xianghe. Therefore, we use the scaling factor of 0.5 with the corresponding value 0.012 s^{-1} to represent the pseudo first-order rate coefficients of HO_2 at Xianghe. The sensitivity simulations considering heterogeneous reactions of trace gases and radicals on aerosols show that the daytime average HO_2 concentration drops by 17%, OH drops by 11%, and RO_2 drops by 14%, which indicates that aerosol uptake of trace gases and radicals are not negligible and the measured aerosol size distributions are needed to accurately calculate heterogeneous reaction rates.

3.4. *RO_x budget analysis based on model results*

Figure 5 shows the average diurnal variation of primary sources and termination sinks of RO_x. The maximum RO_x primary production rate, $P(RO_x)$, is 6.9 ppbv h^{-1}. HONO photolysis is the predominant source of RO_x in the early morning and also a major source throughout the daytime. O_3 photolysis followed by reaction with water vapor, together called the effective photolysis of O_3, and photolysis of HCHO and other carbonyls are the other important RO_x sources at midday. In contrast, alkene ozonolysis dominates the RO_x source during nighttime. In the following, the daytime average (0600 to 1800 LST) will be the focus for the radical budget analysis. The photolysis of HONO and the effective photolysis of O_3 contribute 41% and 20% to $P(RO_x)$, with average production rates of 1.6 ppbv h^{-1} and 0.8 ppbv h^{-1}, respectively, which are also the predominant sources of OH radical, while other OH sources from photolysis of H_2O_2 and HNO_3 are negligible in this study. The photolysis of HCHO and other OVOCs contributes 26% to $P(RO_x)$, with an average production rate of 1.0 ppbv h^{-1}, among which HCHO photolysis produces HO_2 (0.4 ppbv h^{-1}) and other OVOCs photolysis produces HO_2 (0.3 ppbv h^{-1}) and RO_2 (0.3 ppbv h^{-1}). Alkene ozonolysis contributes 13%, with an average contribution of 0.5 ppbv h^{-1} (0.2 ppbv h^{-1} for OH, 0.2 ppbv h^{-1} for HO_2, and 0.1 ppbv h^{-1} for RO_2). Overall, the average daytime $P(RO_x)$ is 3.9 ppbv h^{-1}, and photolysis reactions dominate 87% of the RO_x sources.

Primary RO_x production depends on the intensity of solar radiation as well as NO_x and VOCs levels. Therefore, partitioning of primary RO_x sources is unique in different areas (Xue et al., 2016 and references therein). At Yufa, HCHO photolysis dominates the $P(RO_x)$ due to high concentration of HCHO (on average 10–15 ppbv at daytime, Lu et al., 2013). In Beijing, Hong Kong, and Mexico City, OVOC photolysis (excluding HCHO) is the dominant source because of high OVOC levels (Volkamer et al., 2010; Liu et al., 2012; Xue et al., 2016). In this study, HONO photolysis dominates the $P(RO_x)$ due to high HONO concentration, similar to New York city (Ren et al., 2003) and Wangdu (Tan

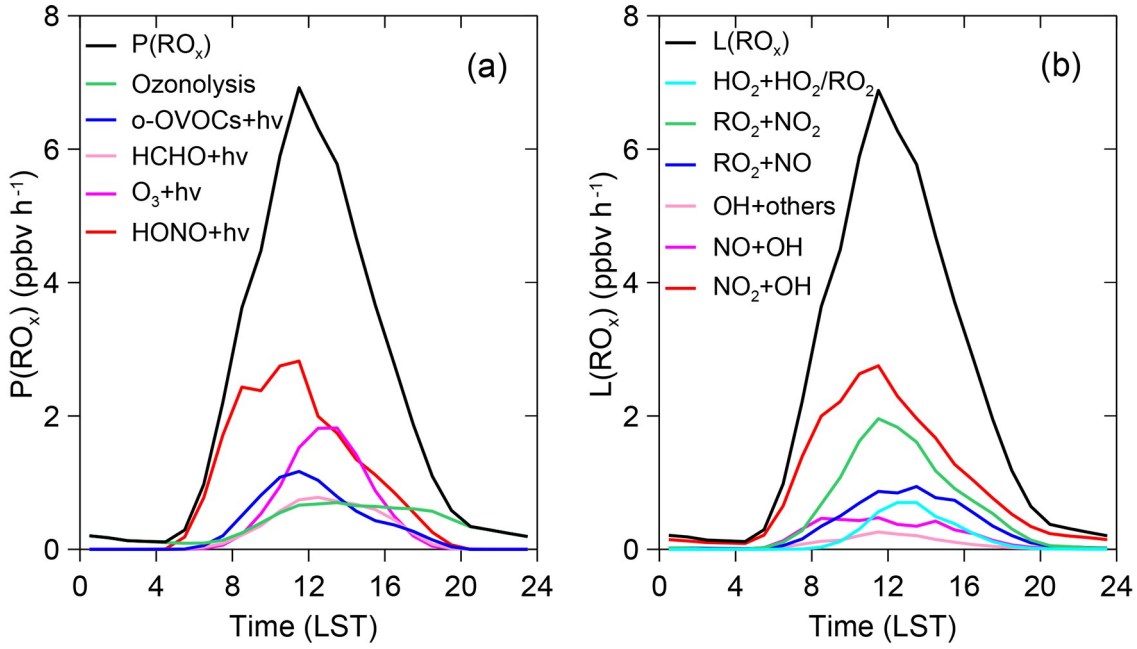

Fig. 5. Averaged diurnal variations of primary sources (a) and termination sinks (b) of RO_x radicals derived from model calculations. The colored lines show the speciated RO_x primary sources and termination sinks. o-OVOCs represent the other OVOC species excluding HCHO. OH + others denotes loss rates by OH with other species (e.g. HNO_3, HNO_2, and HNO_4).

et al., 2017). Sensitivity results without the HONO constraint show that the daytime average $P(RO_x)$ decreases by 55% from 3.9 to 1.7 ppbv h^{-1} (Fig. S3 in the ESM), highlighting the importance of measuring HONO for RO_x budget analysis. In addition to HONO, other radical precursors including HCHO and OVOCs should be measured in future studies since the contributions of their photolysis to the RO_x production are also important in some areas. Sensitivity results considering heterogeneous reactions of trace gases and radicals on aerosols show that there is close to no change in the strength and partition of $P(RO_x)$ (Fig. S4 in the ESM).

Due to the short lifetime of RO_x radicals, the total RO_x loss rate, $L(RO_x)$, is equal to the total RO_x primary production rate, $P(RO_x)$, as shown in Fig. 5b. At the Xianghe site, the radical losses are dominanted by their reactions with NO_x forming nitrogen containing compounds (L_N), including HNO_3, HONO, and PAN-type and $RONO_2$ species, a typical feature of chemistry under high NO_x concentrations. During daytime, the reaction of NO_2 + OH producing HNO_3 is the largest contributor to radical termination (1.6 ppbv h^{-1}, 41%), followed by reactions of RO_2 + NO_2 and RO_2 + NO, producing net PAN-type species (1.0 ppbv h^{-1}, 26%) and $RONO_2$ species (0.5 ppbv h^{-1}, 13%), respectively. In comparison, the radical losses via HO_2 + HO_2/RO_2 reactions forming peroxides (L_H) are much lower (0.3 ppbv h^{-1}, 8%). Contribution of PAN-type species to radical loss is important in urban and suburban areas (Whalley et al., 2018; Tan et al., 2019). According to results found by Whalley et al. (2018), the formation of PAN-type species contributed 30% to the total radical loss in downtown London, similar to the result in this study. Taking into account heterogeneous reactions, aerosol uptake of HO_2 contributes 11% to $L(RO_x)$ for the daytime average (Fig. S4).

The ratio of L_N to $L(RO_x)$ can be used to evaluate the O_3 production sensitivity, as suggested by Kleinman et al. (1997). The threshold of the $L_N/L(RO_x)$ ratio is 0.5. When $L_N/L(RO_x)$ is greater than 0.5, L_N dominates the radical loss, indicating the O_3 production is limited by the VOC abundance. On the other hand, when $L_N/L(RO_x)$ is less than 0.5, the radical loss is dominated by L_H and the O_3 production is controlled by NO_x. The radical budget analysis shows that L_N contributes about 90% to $L(RO_x)$ at Xianghe, which indicates that the O_3 production is in the VOC-sensitive regime.

Figure 6 shows the conversion rates between OH, HO_2, and RO_2 radicals. As shown in Fig. 6a, the conversion of OH to HO_2 is mainly caused by reactions of CO and HCHO with OH. The reactions of speciated VOCs and OVOCs with OH lead to the RO_2 peroxy radicals (Fig. 6b). The conversion of HO_2 from RO_2 is dominated by reactions of isoprene-derived radical (ISOP) and methyl peroxy radical with NO (Fig. 6c). The recycling of OH from HO_2 is mainly generated by the reaction of HO_2 with NO (Fig. 6d). Evidently, the recycling processes between OH, HO_2, and RO_2 are fast at the Xianghe site. For the daytime average, oxidation production rates of HO_2 and RO_2 by OH are 5.6 and 7.2 ppbv h^{-1}, respectively. The reactions of RO_2 + NO and HO_2 + NO further recycle HO_2 and OH, with the corresponding production rates of 6.5 ppbv h^{-1} and 12.5 ppbv h^{-1}, respectively. In polluted areas under the coexistence of abundant VOCs and NO_x, efficient radical recycling can amplify the

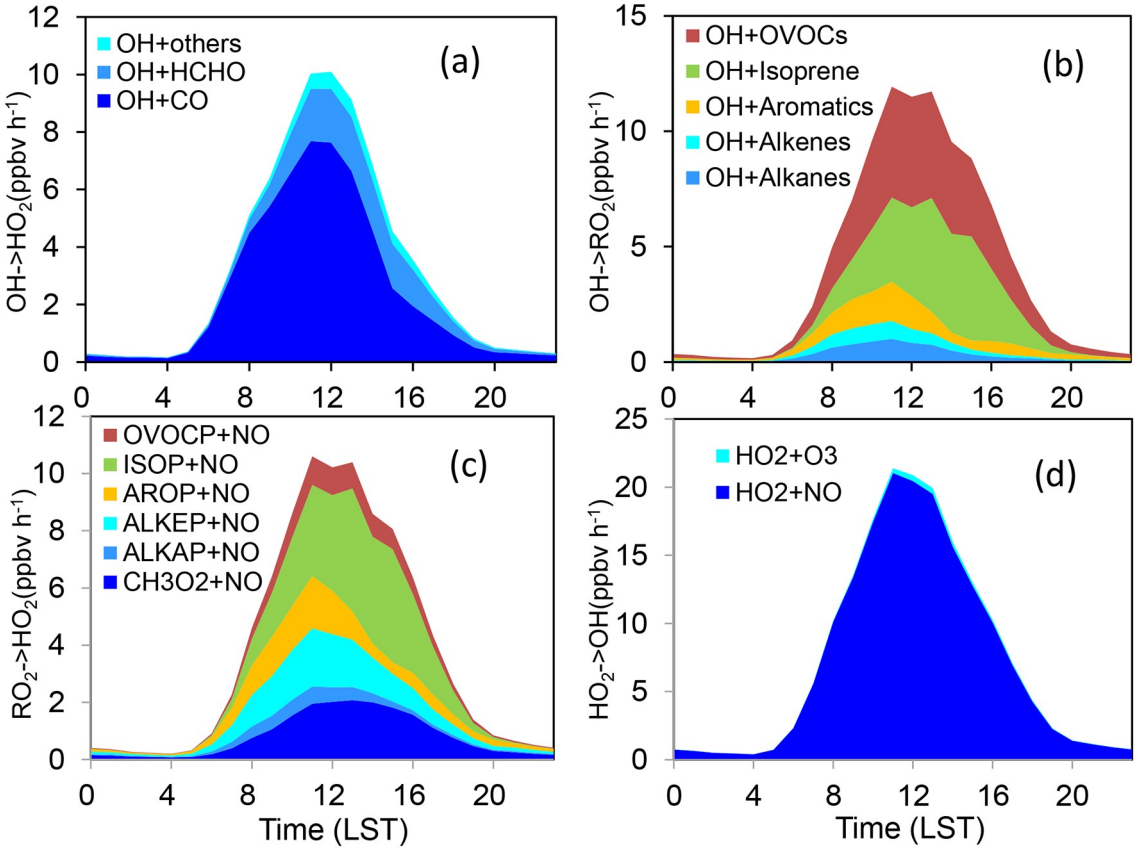

Fig. 6. Averaged diurnal variations of radical conversion rates of $OH \rightarrow HO_2$ (a), $OH \rightarrow RO_2$ (b), $RO_2 \rightarrow HO_2$ (c), and $HO_2 \rightarrow OH$ (d). (a): OH + others denotes conversion rates by the reaction of OH with other species (e.g. H_2, O_3, and C_6H_6).

effect of the initially produced radicals (Ma et al., 2012; Xue et al., 2016).

3.5. *O_3 photochemical production and loss*

The photolysis of NO_2 produces O_3 and NO. NO titrates O_3 to regenerate NO_2. These reactions represent a null cycle for O_3 production in sunlight because there is no change in O_3 abundance at steady state. The removal of NO without consuming O_3 leads to net O_3 production. In the photochemical system, HO_2 and RO_2 radicals are the major NO consumers and O_3 is produced via the reactions of NO with HO_2 and RO_2 radicals. On the other hand, O_3 chemical loss occurs via O_3 photolysis (production of O^1D, followed by reaction with water vapor) and reactions with OH, HO_2, and alkenes. The reaction of NO_2 with OH should also be considered as O_3 chemical loss because the conversion of NO_2 to HNO_3 terminates the catalytic cycle between NO and NO_2. As in previous studies (Liu et al., 1987; Lu et al., 2010; Xue et al., 2013), the total oxidant ($O_x = O_3 + NO_2$) is used to calculate instantaneous O_3 photochemical formation rate $F(O_3)$ and loss rate $L(O_3)$, as denoted in Eqs. (2) and (3),

$$F(O_3) = K_{HO_2+NO}[HO_2][NO] + \sum K_{RO_2+NO}[RO_2][NO], \quad (2)$$

$$L(O_3) = \left[O^1D\right][H_2O] + (K_{O_3+OH}[OH] + K_{O_3+HO_2}[HO_2] + K_{O_3+Alkene}[Alkene])[O_3] + K_{NO_2+OH}[NO_2][OH], \quad (3)$$

where [OH], [HO_2], [RO_2], [O^1D], [NO], [O_3], and [Alkene] are concentrations, and K represents the rate coefficient of the corresponding reaction. The net O_3 photochemical production rate $P(O_3)$ is the difference between the $F(O_3)$ and $L(O_3)$. Figure 7 shows the average diurnal variations of $F(O_3)$ and $L(O_3)$ calculated with the model simulated radical concentrations. The average diurnal maximum $F(O_3)$ is 32.9 ppbv h^{-1} at 1100 LST. The reaction of HO_2 + NO is the dominant process resulting in O_3 production. For the daytime average (0600–1800 LST), the reaction of HO_2 + NO contributes about 62% to the total O_3 production, which is consistent with previous results (Liu et al., 2012; Ma et al., 2012; Tan et al., 2019). The reaction of ISOP with NO accounts for about 11% of the total O_3 production due to relatively high isoprene and ISOP peroxy radical concentration at the Xianghe site, followed by the reaction of CH_3O_2 with NO (7%).

Using an observation-based model, Lu et al (2010) calculated the hourly $F(O_3)$, varying from zero to 120 and 50 ppbv h^{-1} at PKU and Yufa sites, respectively, during summer 2006 in Beijing. Liu et al (2012) simulated the average diurnal maximum $F(O_3)$ of 60 ppbv h^{-1} at PKU during sum-

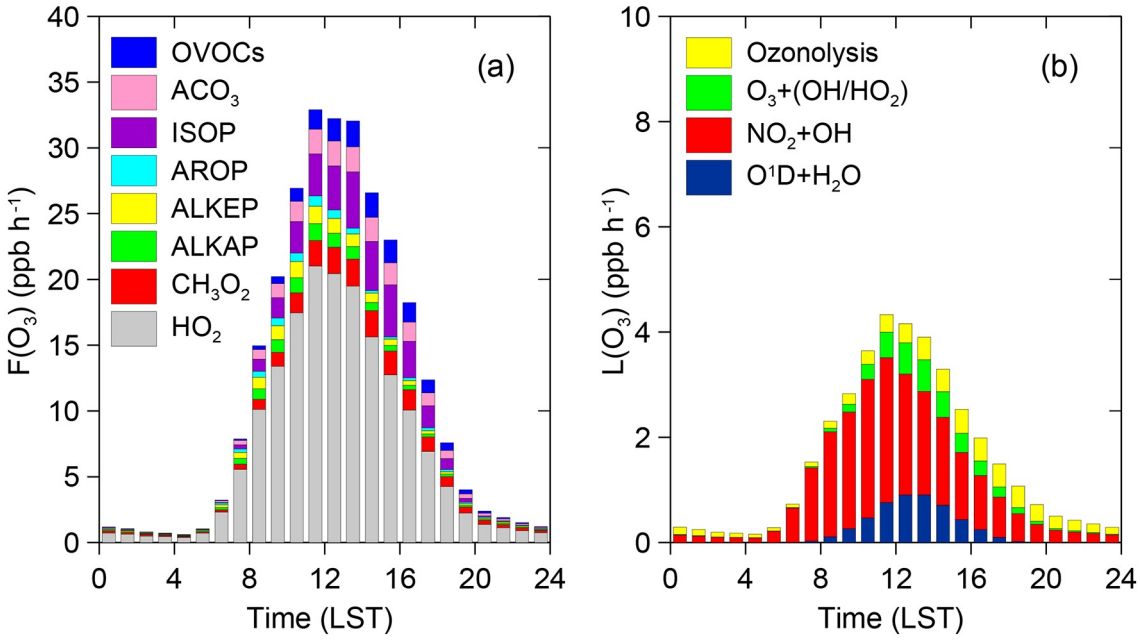

Fig. 7. Averaged diurnal variations of O_3 production (a) and loss rate (b) derived from model calculations. The left panel represents the speciated O_3 formation rate from different RO_2 species. The right panel represents the speciated O_3 destruction rate.

mer 2007. Tan et al (2018) reported the average diurnal maximum $F(O_3)$ was 17 ppbv h^{-1} at Wangdu during summer 2014. The maximum $F(O_3)$ at Xianghe lies between the simulated results at rural site Wangdu and urban site PKU. The RO_x radical concentrations at Xianghe are comparable to Wangdu and PKU as mentioned in section 3.3, while the corresponding noontime NO concentrations are 2.3 ppbv, 0.16 ppbv, and 5.0 ppbv at Xianghe, Wangdu, and PKU, respectively, resulting in the difference in the $F(O_3)$ which depends on both RO_x and NO as shown in Eq. 2.

The average diurnal maximum $L(O_3)$ is 4.3 ppbv h^{-1}, appearing at 1100 LST. The reaction of NO_2 + OH is the main process leading to O_3 chemical loss, with a contribution of 63% toward the daytime average. The effective photolysis of O_3 and alkene ozonolysis contribute to 15% and 12%, respectively. By integrating the difference between the photochemical formation and loss rates over the whole day, the $P(O_3)$ approaches 237 ppbv d^{-1}, indicating that the photochemical production of O_3 is active at the suburban site in the NCP region.

The sensitivity results without the HONO constraint show that average diurnal maximum $F(O_3)$ decreases from 32.9 to 22.6 ppbv h^{-1} (Fig. S5 in the ESM). The daytime average $F(O_3)$ decreases by 42%, consistent with the results reported by Liu et al (2012). Therefore, it is necessary to constrain the photochemical models with the measured HONO data. The sensitivity results considering heterogeneous reactions show that average diurnal maximum $F(O_3)$ decreases to 28.4 ppbv h^{-1} (Fig. S5 in the ESM). The daytime average $F(O_3)$ decreases by 14%, about one third of the results without the HONO constraint, indicating that aerosol size distributions should be measured to accurately calculate heterogeneous reaction rates and O_3 photochemical formation.

3.6. *Chemical regimes of O_3 production*

The O_3-NO_x-VOCs sensitivity is investigated using the Empirical Kinetic Modelling Approach (EKMA). The base case refers to the averaged conditions over the whole campaign during the daytime. The averaged chemical and physical parameters are summarized in Table S2 in the ESM. By increasing or decreasing the concentrations of NO_x and AVOCs up to a factor of 3 with 30 equal-distance steps and fixing all other parameters as in the base case, the corresponding O_3 production rates are calculated and used to generate an isopleth plot illustrating the $P(O_3)$ on the concentration of NO_x and AVOCs. The change of VOCs concentrations only applies to AVOCs to investigate the impact of anthropogenic emission changes on $P(O_3)$.

Figure 8 shows the response of $P(O_3)$ to precursors of NO_x and VOCs at the Xianghe site. The O_3 chemical regimes between VOC-sensitive and NO_x-sensitive are separated by the black line, also called the ridge line. The ridge line connects the turning points of the $P(O_3)$ isopleths and represents the optimum initial NO_x and VOC concentrations for O_3 production. Above the ridge line, a reduction in initial NO_x results in an increase in the $P(O_3)$, whereas a reduction in initial VOC results in a decrease in the $P(O_3)$, and this condition is considered VOC-sensitive. Below the ridge line, a reduction in initial VOC has only a very small effect on the $P(O_3)$, whereas $P(O_3)$ is reduced by reduction in the initial NO_x, and this condition is considered NO_x-sensitive. The black filled square in the isopleth diagrams represents the daytime averaged NO_x and AVOCs concentrations for the time period of 1–23 July, and blue circles stand for the

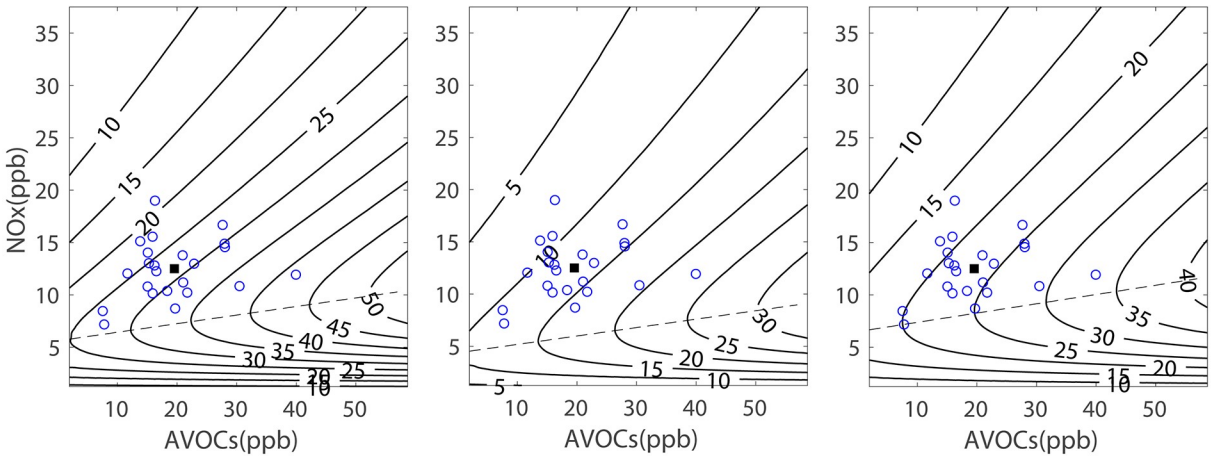

Fig. 8. Isopleth diagrams of the net O_3 production rate [$P(O_3)$, units: ppb h^{-1}] as functions of the NO_x and AVOCs derived from an empirical kinetic modeling approach. The black filled squares represent the daytime averaged NO_x and AVOCs concentrations measured for the time period of 1–23 July. The blue circles represent daytime averaged AVOCs and NO_x concentrations measured for each day. The left panel represents the EKMA diagram with all measured gases as model constraints; the middle panel represents the EKMA diagram without the HONO constraint; the right panel represents the EKMA diagram considering heterogeneous reactions of gases and radicals on aerosols.

daytime averaged NO_x and AVOCs concentrations for each day. The filled square and most of the circles are above the ridge line, indicating that the O_3 production is mainly controlled by VOCs. This conclusion is consistent with the result from radical loss analysis in section 3.4. Compared to Xianghe, O_3 formation at Wangdu was NO_x-sensitive due to lower NO_x levels during daytime (Tan et al., 2018). This radical loss process was further verified by the fact that the radical loss was dominated by HO_2 + HO_2/RO_2 reactions at Wangdu, representing a NO_x-sensitive regime (Tan et al., 2017). When the NO_x concentration is larger than 10 ppbv, the calculated $P(O_3)$ decreases with increasing NO_x, demonstrating that O_3 production enters the NO_x titration regime.

The impact of HONO and aerosol uptake of trace gases and radicals on $P(O_3)$ chemical regimes is also investigated as part of this study. As shown in Fig. 8, without the HONO constraint, the ridge moves down and all circles are above the ridge line, which means that the O_3 formation is more VOC-sensitive. The aerosol uptake of trace gases and radicals makes the ridge move up as shown in Fig. 8, whereas the filled square and most of the circles are still above the ridge line, which means that the O_3 production is unchanged but has a tendency shifting toward NO_x-sensitive. Therefore, VOCs control should be the optimal way to mitigate the O_3 pollution at Xianghe.

4. Conclusions

We present the measurements of O_3, NO_x, CO, VOCs, and HONO and major physical parameters at the Xianghe suburban site located in the NCP region during summer 2018. Using a chemical box model constrained by these measurement data, we investigate the radical budget, O_3 photochemical production and loss, and the O_3-VOC-NO_x sensitivity based on the EKMA approach. We further discuss the sensitivity of HONO and heterogeneous reactions of radicals on the radical budget and O_3 photochemical production.

Results show that mean concentrations plus/minus standard deviations of O_3, O_x, NO, NO_x, CO, AVOC, Isoprene, and HONO are 46.1 ± 28.8 ppbv, 57.2 ± 26.5 ppbv, 1.9 ± 1.8 ppbv, 13.0 ± 6.0 ppbv, 694.6 ± 478.1 ppbv, 20.1 ± 11.0 ppbv, 0.7 ± 0.9 ppbv, and 1.0 ± 0.5 ppbv, respectively. Additionally, the OH reactivity values vary between 12 s^{-1} and 18 s^{-1}, with average K_{OH} of 15.0 s^{-1}.

The average diurnal maximum RO_x primary production rate, $P(RO_x)$, is 6.9 ppbv h^{-1}. For the daytime average, the total RO_x primary production rate is 3.9 ppbv h^{-1}. Photolysis reactions dominate 87% (41% for HONO photolysis, 20% for O_3 photolysis, and 26% for OVOC photolysis) of the primary radical sources, and alkene ozonolysis contributes 13%. The radical termination is dominated by the reaction of OH with NO_x, representing the VOC-sensitive regime at Xianghe site.

The average diurnal maximum chemical production of O_3 is 32.9 ppbv h^{-1}, and the maximum chemical loss of O_3 is 4.3 ppbv h^{-1}. The reaction of HO_2 with NO is the main process for O_3 production, contributing about 62% to the total O_3 production for the daytime average. O_3 loss is dominated by reaction of NO_2 with OH, with a contribution of 63%.

Sensitivity tests without the HONO constraint point to decreases in the daytime average primary RO_x production rate by 55%, and O_3 photochemical production by 42%, highlighting the importance of measuring HONO for quantifying RO_x budget and O_3 photochemical production. Taking into account aerosol uptake of trace gases and radicals, aerosol uptake of HO_2 contributes 11% to RO_x sink, and the daytime average $F(O_3)$ decreases by 14%, indicating that aerosol size distributions should be measured to accurately calculate heterogeneous reaction rates and O_3 photochemical forma-

tion. EKMA contour suggests that the O_3 production in suburban Beijing lies in the VOC-sensitive regime, where reduction of VOCs could lead to reduced O_3 production. Sensitivity test results without the HONO constraint over-emphasize the VOC-sensitive effect on the O_3 production. Considering aerosol uptake of trace gases and radicals, the O_3 production regime remains unchanged but has a tendency shifting toward being NO_x-sensitive.

Acknowledgements. This work was supported by grants from the National Key Research and Development Program of China (Grant No. 2017YFC0210003). The authors are grateful to all staff and workers from the Xianghe Atmospheric Observatory of Institute of Atmospheric Physics (IAP) of the Chinese Academy of Sciences for their support during the sampling campaign.

Electronic supplementary material: Supplementary material is available in the online version of this article at https://doi.org/10.1007/s00376-021-0327-4.

REFERENCES

Atkinson, R., and J. Arey, 2003: Atmospheric degradation of volatile organic compounds. *Chemical Reviews*, **103**, 4605–4638, https://doi.org/10.1021/cr0206420.

Dolgorouky, C., and Coauthors, 2012: Total OH reactivity measurements in Paris during the 2010 MEGAPOLI winter campaign. *Atmospheric Chemistry and Physics*, **12**, 9593–9612, https://doi.org/10.5194/acp-12-9593-2012.

Ehhalt, D. H., 1999: Photooxidation of trace gases in the troposphere Plenary Lecture. *Physical Chemistry Chemical Physics*, **1**, 5401–5408, https://doi.org/10.1039/A905097C.

Elshorbany, Y. F., B. Steil, C. Brühl, and J. Lelieveld, 2012: Impact of HONO on global atmospheric chemistry calculated with an empirical parameterization in the EMAC model. *Atmospheric Chemistry and Physics*, **12**, 9977–10000, https://doi.org/10.5194/acp-12-9977-2012.

Emmerson, K. M., N. Carslaw, and M. J. Pilling, 2005a: Urban atmospheric chemistry during the PUMA campaign 2: Radical budgets for OH, HO_2 and RO_2. *Journal of Atmospheric Chemistry*, **52**, 165–183, https://doi.org/10.1007/s10874-005-1323-2.

Emmerson, K. M., N. Carslaw, L. J. Carpenter, D. E. Heard, J. D. Lee, and M. J. Pilling, 2005b: Urban atmospheric chemistry during the PUMA Campaign 1: Comparison of modelled OH and HO_2 concentrations with measurements. *Journal of Atmospheric Chemistry*, **52**, 143–164, https://doi.org/10.1007/s10874-005-1322-3.

Fuchs, H., and Coauthors, 2017: OH reactivity at a rural site (Wangdu) in the North China Plain: Contributions from OH reactants and experimental OH budget. *Atmospheric Chemistry and Physics*, **17**, 645–661, https://doi.org/10.5194/acp-17-645-2017.

Hofzumahaus, A., and Coauthors, 2009: Amplified trace gas removal in the troposphere. *Science*, **324**, 1702–1704, https://doi.org/10.1126/science.1164566.

Hou, S. Q., S. R. Tong, M. F. Ge, and J. L. An, 2016: Comparison of atmospheric nitrous acid during severe haze and clean periods in Beijing, China. *Atmos. Environ.*, **124**, 199–206, https://doi.org/10.1016/j.atmosenv.2015.06.023.

Ji, D. S., and Coauthors, 2014: The heaviest particulate air-pollution episodes occurred in northern China in January, 2013: Insights gained from observation. *Atmos. Environ.*, **92**, 546–556, https://doi.org/10.1016/j.atmosenv.2014.04.048.

Kleffmann, J., J. Heland, R. Kurtenbach, J. C. Lörzer, and P. Wiesen, 2002: A new instrument (LOPAP) for the detection of nitrous acid (HONO). *Environmental Science and Pollution Research*, **9**, 48–54, https://doi.org/10.1007/BF02987316.

Kleinman, L. I., and Coauthors, 1997: Dependence of ozone production on NO and hydrocarbons in the troposphere. *Geophys. Res. Lett.*, **24**, 2299–2302, https://doi.org/10.1029/97GL02279.

Kubistin, D., and Coauthors, 2010: Hydroxyl radicals in the tropical troposphere over the Suriname rainforest: Comparison of measurements with the box model MECCA. *Atmospheric Chemistry and Physics*, **10**, 9705–9728, https://doi.org/10.5194/acp-10-9705-2010.

Kuhn, U., and Coauthors, 2010: Impact of Manaus City on the Amazon Green Ocean atmosphere: ozone production, precursor sensitivity and aerosol load. *Atmospheric Chemistry and Physics*, **10**, 9251–9282, https://doi.org/10.5194/acp-10-9251-2010.

Lelieveld, J., 2010: Atmospheric chemistry: A missing sink for radicals. *Nature*, **466**, 925–926, https://doi.org/10.1038/466925a.

Levy, H., 1971: Normal atmosphere: Large radical and formaldehyde concentrations predicted. *Science*, **173**, 141–143, https://doi.org/10.1126/science.173.3992.141.

Li, G. H., and Coauthors, 2017: Widespread and persistent ozone pollution in eastern China during the non-winter season of 2015: observations and source attributions. *Atmospheric Chemistry and Physics*, **17**, 2759–2774, https://doi.org/10.5194/acp-17-2759-2017.

Li, K., D. J. Jacob, H. Liao, L. Shen, Q. Zhang, and K. H. Bates, 2019: Anthropogenic drivers of 2013–2017 trends in summer surface ozone in China. *Proceedings of the National Academy of Sciences of the United States of America*, **116**, 422–427, https://doi.org/10.1073/pnas.1812168116.

Li, X., and Coauthors, 2014: Missing gas-phase source of HONO inferred from zeppelin measurements in the troposphere. *Science*, **344**, 292–296, https://doi.org/10.1126/science.1248999.

Lin, W., X. Xu, X. Zhang, and J. Tang, 2008: Contributions of pollutants from North China Plain to surface ozone at the Shangdianzi GAW Station. *Atmospheric Chemistry and Physics*, **8**, 5889–5898, https://doi.org/10.5194/acp-8-5889-2008.

Liu, J. Y., and Coauthors, 2021: Detailed budget analysis of HONO in Beijing, China: Implication on atmosphere oxidation capacity in polluted megacity. *Atmos. Environ.*, **244**, 117957, https://doi.org/10.1016/j.atmosenv.2020.117957.

Liu, S. C., M. Trainer, F. C. Fehsenfeld, D. D. Parrish, E. J. Williams, D. W. Fahey, G. Hübler, and P. C. Murphy, 1987: Ozone production in the rural troposphere and the implications for regional and global ozone distributions. *J. Geophys. Res.*, **92**, 4191–4207, https://doi.org/10.1029/JD092iD04p04191.

Liu, Z., and Coauthors, 2012: Summertime photochemistry during CAREBeijing-2007: RO_x budgets and O_3 formation. *Atmospheric Chemistry and Physics*, **12**, 7737–7752, https://doi.org/10.5194/acp-12-7737-2012.

Lou, S., and Coauthors, 2010: Atmospheric OH reactivities in the

Pearl River Delta -China in summer 2006: Measurement and model results. *Atmospheric Chemistry and Physics*, **10**, 11243–11260, https://doi.org/10.5194/acp-10-11243-2010.

Lu, K. D., and Coauthors, 2010: Oxidant (O_3 + NO_2) production processes and formation regimes in Beijing. *J. Geophys. Res.*, **115**, D07303, https://doi.org/10.1029/2009JD012714.

Lu, K. D., and Coauthors, 2012: Observation and modelling of OH and HO_2 concentrations in the Pearl River Delta 2006: A missing OH source in a VOC rich atmosphere. *Atmospheric Chemistry and Physics*, **12**, 1541–1569, https://doi.org/10.5194/acp-12-1541-2012.

Lu, K. D., and Coauthors, 2013: Missing OH source in a suburban environment near Beijing: Observed and modelled OH and HO_2 concentrations in summer 2006. *Atmospheric Chemistry and Physics*, **13**, 1057–1080, https://doi.org/10.5194/acp-13-1057-2013.

Lu, X., and Coauthors, 2018: Severe surface ozone pollution in China: A global perspective. *Environmental Science & Technology Letters*, **5**, 487–494, https://doi.org/10.1021/acs.estlett.8b00366.

Lu, X., and Coauthors, 2019: Exploring 2016-2017 surface ozone pollution over China: Source contributions and meteorological influences. *Atmospheric Chemistry and Physics*, **19**, 8339–8361, https://doi.org/10.5194/acp-19-8339-2019.

Ma, J. Z., J. Tang, X. J. Zhou, and X. S. Zhang, 2002: Estimates of the chemical budget for ozone at waliguan observatory. *Journal of Atmospheric Chemistry*, **41**, 21–48, https://doi.org/10.1023/A:1013892308983.

Ma, J. Z., and Coauthors, 2012: The IPAC-NC field campaign: A pollution and oxidization pool in the lower atmosphere over Huabei, China. *Atmospheric Chemistry and Physics*, **12**, 3883–3908, https://doi.org/10.5194/acp-12-3883-2012.

Ma, J. Z., W. Wang, H. J. Liu, Y. Chen, X. B. Xu, and J. Lelieveld, 2013: Pollution plumes observed by aircraft over North China during the IPAC-NC field campaign. *Chinese Science Bulletin*, **58**, 4329–4336, https://doi.org/10.1007/s11434-013-5978-9.

Ma, Z. Q., J. Xu, W. J. Quan, Z. Y. Zhang, W. L. Lin, and X. B. Xu, 2016: Significant increase of surface ozone at a rural site, north of eastern China. *Atmospheric Chemistry and Physics*, **16**, 3969–3977, https://doi.org/10.5194/acp-16-3969-2016.

Madronich, S., and J. G. Calvert, 1990: Permutation reactions of organic peroxy radicals in the troposphere. *Journal of Geophysical Research*, **95**, 5697–5715, https://doi.org/10.1029/JD095iD05p05697.

Mao, J., and Coauthors, 2010: Chemistry of hydrogen oxide radicals (HO_x) in the Arctic troposphere in spring. *Atmospheric Chemistry and Physics*, **10**, 5823–5838, https://doi.org/10.5194/acp-10-5823-2010.

Molina, L. T., and Coauthors, 2010: An overview of the MILAGRO 2006 Campaign: Mexico City emissions and their transport and transformation. *Atmospheric Chemistry and Physics*, **10**, 8697–8760, https://doi.org/10.5194/acp-10-8697-2010.

Molina, M. J., and L. T. Molina, 2004: Megacities and atmospheric pollution. *Journal of the Air & Waste Management Association*, **54**, 644–680, https://doi.org/10.1080/10473289.2004.10470936.

Monks, P. S., and Coauthors, 2009: Atmospheric composition change—Global and regional air quality. *Atmos. Environ.*, **43**, 5268–5350, https://doi.org/10.1016/j.atmosenv.2009.08.021.

Monks, P. S., and Coauthors, 2015: Tropospheric ozone and its precursors from the urban to the global scale from air quality to short-lived climate forcer. *Atmospheric Chemistry and Physics*, **15**, 8889–8973, https://doi.org/10.5194/acp-15-8889-2015.

Qu, Y., J. L. An, J. Li, Y. Chen, Y. Li, X. G. Liu, and M. Hu, 2014: Effects of NO_x and VOCs from five emission sources on summer surface O_3 over the Beijing-Tianjin-Hebei region. *Adv. Atmos. Sci.*, **31**, 787–800, https://doi.org/10.1007/s00376-013-3132-x.

Ren, X. R., and Coauthors, 2003: OH and HO_2 Chemistry in the urban atmosphere of New York City. *Atmos. Environ.*, **37**, 3639–3651, https://doi.org/10.1016/S1352-2310(03)00459-X.

Shao, M., S. H. Lu, Y. Liu, X. Xie, C. C. Chang, S. Huang, and Z. M. Chen, 2009: Volatile organic compounds measured in summer in Beijing and their role in ground-level ozone formation. *J. Geophys. Res.*, **114**, D00G06, https://doi.org/10.1029/2008JD010863.

Sheehy, P. M., R. Volkamer, L. T. Molina, and M. J. Molina, 2010: Oxidative capacity of the Mexico City atmosphere—Part 2: A RO_x radical cycling perspective. *Atmospheric Chemistry and Physics*, **10**, 6993–7008, https://doi.org/10.5194/acp-10-6993-2010.

Shirley, T. R., and Coauthors, 2006: Atmospheric oxidation in the Mexico City Metropolitan Area (MCMA) during April 2003. *Atmospheric Chemistry and Physics*, **6**, 2753–2765, https://doi.org/10.5194/acp-6-2753-2006.

Stone, D., L. K. Whalley, and D. E. Heard, 2012: Tropospheric OH and HO_2 radicals: Field measurements and model comparisons. *Chemical Society Reviews*, **41**, 6348–6404, https://doi.org/10.1039/C2CS35140D.

Streets, D. G., and Coauthors, 2007: Air quality during the 2008 Beijing Olympic Games. *Atmos. Environ.*, **41**, 480–492, https://doi.org/10.1016/j.atmosenv.2006.08.046.

Su, H., and Coauthors, 2011: Soil nitrite as a source of atmospheric HONO and OH radicals. *Science*, **333**, 1616–1618, https://doi.org/10.1126/science.1207687.

Sun, L., and Coauthors, 2016: Significant increase of summertime ozone at Mount Tai in Central Eastern China. *Atmospheric Chemistry and Physics*, **16**, 10637–10650, https://doi.org/10.5194/acp-16-10637-2016.

Tan, Z. F., and Coauthors, 2017: Radical chemistry at a rural site (Wangdu) in the North China Plain: Observation and model calculations of OH, HO_2 and RO_2 radicals. *Atmospheric Chemistry and Physics*, **17**, 663–690, https://doi.org/10.5194/acp-17-663-2017.

Tan, Z. F., and Coauthors, 2018: Explicit diagnosis of the local ozone production rate and the ozone-NO_x-VOC sensitivities. *Science Bulletin*, **63**, 1067–1076, https://doi.org/10.1016/j.scib.2018.07.001.

Tan, Z. F., and Coauthors, 2019: Daytime atmospheric oxidation capacity in four Chinese megacities during the photochemically polluted season: A case study based on box model simulation. *Atmospheric Chemistry and Physics*, **19**, 3493–3513, https://doi.org/10.5194/acp-19-3493-2019.

Tang, G. Q., and Coauthors, 2016: Mixing layer height and its implications for air pollution over Beijing, China. *Atmospheric Chemistry and Physics*, **16**, 2459–2475, https://doi.org/10.5194/acp-16-2459-2016.

Tang, G. Q., and Coauthors, 2019: Decreased gaseous carbonyls

in the North China plain from 2004 to 2017 and future control measures. *Atmos. Environ.*, **218**, 117015, https://doi.org/10.1016/j.atmosenv.2019.117015.

Tang, G., X. Li, Y. Wang, J. Xin, and X. Ren, 2009: Surface ozone trend details and interpretations in Beijing, 2001–2006. *Atmospheric Chemistry and Physics*, **9**, 8813–8823, https://doi.org/10.5194/acp-9-8813-2009.

Tang, G., Y. Wang, X. Li, D. Ji, S. Hsu, and X. Gao, 2012: Spatial-temporal variations in surface ozone in Northern China as observed during 2009–2010 and possible implications for future air quality control strategies. *Atmospheric Chemistry and Physics*, **12**, 2757–2776, https://doi.org/10.5194/acp-12-2757-2012.

Tong, S. R., S. Q. Hou, Y. Zhang, B. W. Chu, Y. C. Liu, H. He, P. S. Zhao, and M. F. Ge, 2016: Exploring the nitrous acid (HONO) formation mechanism in winter Beijing: Direct emissions and heterogeneous production in urban and suburban areas. *Faraday Discussions*, **189**, 213–230, https://doi.org/10.1039/C5FD00163C.

Volkamer, R., P. Sheehy, L. T. Molina, and M. J. Molina, 2010: Oxidative capacity of the Mexico City atmosphere- Part 1: A radical source perspective. *Atmospheric Chemistry and Physics*, **10**, 6969–6991, https://doi.org/10.5194/acp-10-6969-2010.

Wang, M., and Coauthors, 2014: Development and validation of a cryogen-free automatic gas chromatograph system (GC-MS/FID) for online measurements of volatile organic compounds. *Analytical Methods*, **6**, 9424–9434, https://doi.org/10.1039/C4AY01855A.

Wang, T., A. J. Ding, J. Gao, and W. S. Wu, 2006: Strong ozone production in urban plumes from Beijing, China. *Geophys. Res. Lett.*, **33**, L21806, https://doi.org/10.1029/2006GL027689.

Wang, T., X. L. Wei, A. J. Ding, C. N. Poon, K. S. Lam, Y. S. Li, L. Y. Chan, and M. Anson, 2009: Increasing surface ozone concentrations in the background atmosphere of Southern China, 1994–2007. *Atmospheric Chemistry and Physics*, **9**, 6217–6227, https://doi.org/10.5194/acp-9-6217-2009.

Wang, T., L. K. Xue, P. Brimblecombe, Y. F. Lam, L. Li, and L. Zhang, 2017: Ozone pollution in China: A review of concentrations, meteorological influences, chemical precursors, and effects. *Science of The Total Environment*, **575**, 1582–1596, https://doi.org/10.1016/j.scitotenv.2016.10.081.

Whalley, L. K., and Coauthors, 2018: Understanding in situ ozone production in the summertime through radical observations and modelling studies during the Clean air for London project (ClearfLo). *Atmospheric Chemistry and Physics*, **18**, 2547–2571, https://doi.org/10.5194/acp-18-2547-2018.

Williams, J., and Coauthors, 2016: Opposite OH reactivity and ozone cycles in the Amazon rainforest and megacity Beijing: Subversion of biospheric oxidant control by anthropogenic emissions. *Atmos. Environ.*, **125**, 112–118, https://doi.org/10.1016/j.atmosenv.2015.11.007.

Wu, J. R., and Coauthors, 2017: Contributions of trans-boundary transport to summertime air quality in Beijing, China. *Atmospheric Chemistry and Physics*, **17**, 2035–2051, https://doi.org/10.5194/acp-17-2035-2017.

Xu, J., and Coauthors, 2011: Measurements of ozone and its precursors in Beijing during summertime: Impact of urban plumes on ozone pollution in downwind rural areas. *Atmospheric Chemistry and Physics*, **11**, 12241–12252, https://doi.org/10.5194/acp-11-12241-2011.

Xue, L. K., and Coauthors, 2016: Oxidative capacity and radical chemistry in the polluted atmosphere of Hong Kong and Pearl River Delta region: Analysis of a severe photochemical smog episode. *Atmospheric Chemistry and Physics*, **16**, 9891–9903, https://doi.org/10.5194/acp-16-9891-2016.

Xue, M., J. Z. Ma, Y. Li, S. Zhu, B. Zhao, P. Yan, G. A. Ding, and R. J. Jin, 2013: Chemical characteristics of air masses from different urban and industrial centers in the Huabei region of China. *Atmos. Environ.*, **71**, 122–130, https://doi.org/10.1016/j.atmosenv.2013.01.045.

Yang, Y. D., and Coauthors, 2017: How the OH reactivity affects the ozone production efficiency: Case studies in Beijing and Heshan, China. *Atmospheric Chemistry and Physics*, **17**, 7127–7142, https://doi.org/10.5194/acp-17-7127-2017.

Zhang, Q., and Coauthors, 2014: Variations of ground-level O_3 and its precursors in Beijing in summertime between 2005 and 2011. *Atmospheric Chemistry and Physics*, **14**, 6089–6101, https://doi.org/10.5194/acp-14-6089-2014.

Zhang, Y. H., and Coauthors, 2008: Regional ozone pollution and observation-based approach for analyzing ozone-precursor relationship during the PRIDE-PRD2004 campaign. *Atmos. Environ.*, **42**, 6203–6218, https://doi.org/10.1016/j.atmosenv.2008.05.002.

Zhao, S., and Coauthors, 2021: Photolysis rate in the Beijing-Tianjin-Hebei region: Reconstruction and long-term trend. *Atmospheric Research*, **256**, 105568, https://doi.org/10.1016/j.atmosres.2021.105568.